Engineering Structures 318 (2024) 118748

Contents lists available at ScienceDirect

Engineering Structures

journal homepage: www.elsevier.com/locate/engstruct

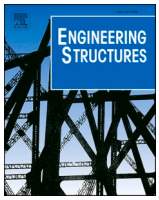

Impact resistance and performance of precast shear walls with various connections under axial and lateral loads

Yun Zhou [a], Xin Zhang [b], Fan Yi [b], Jing-Ming Sun [b,*], Jia Ni [b], Ting Li [b], Wei-Jian Yi [a]

[a] College of Civil Engineering, Hunan Provincial Key Lab on Damage Diagnosis for Engineering Structures, Hunan University, Changsha 410082,China
[b] College of Civil Engineering, Hunan University, Changsha 410082, China

ARTICLE INFO

Keywords:
Precast concrete shear wall
Various connections
Experimental study
Impact loading
Constant axial force loading

ABSTRACT

This study conducted pendulum impact tests on three precast concrete (PC) shear wall specimens with various connection types and one cast-in-situ reinforced concrete (RC) shear wall specimen to investigate their behavior under out-of-plane impact loads at a consistent axial compression ratio. The study reported observations on failure patterns, the progression of cracks, the dynamics of impact force over time, relationships between axial force and vertical displacement, deformation behavior, and the strains in concrete and rebars. Through comparative analysis with similar PC columns, the influence of various connections on the impact resistance is analyzed for both shear walls and column specimens. It was found that all PC specimens showed flexural failure modes akin to those of the RC specimen, yet with more extensive cracking and lower stiffness. PC specimens with grouted sleeve connections demonstrated satisfying impact resistance that emulates the performance of cast-in-situ walls. Specimens with grouted corrugated metallic duct connections demonstrated obvious localized damage. Eventually, the study proposes a novel method for rapidly evaluation of the impact resistance of concrete shear walls.

1. Introduction

Precast concrete (PC) structures are characterized by the industrialization and standardization that enhances efficiency and quality assurance during the construction process. In PC structures, the connection design plays a crucial role in the synergistic work between components and the transmission of loads. Currently, the connection methods in PC structures can be categorized as either dry or wet connections, distinguished by whether the concrete is poured in-situ at connections.

Contemporarily, wet connections are preferred in engineering practices of PC shear walls for their excellent stress transfer capabilities that can emulate cast-in-situ construction while assuring grouting quality can be achieved [1]. Literatures suggest that wet-connected PC shear walls closely match the performance of their cast-in-situ counterparts in numerous respects [2–10]. Notably: Xue et al. [2–4] reported that PC shear walls are more superior in terms of hysteresis behavior, displacement ductility, and energy absorption; Jiang et al. [5,6] observed higher ductility in PC walls; and Wu et al. [8] highlighted denser cracking in cast-in-situ walls. Fan et al. [11] and Chen et al. [12] suggest that the shear performance of PC shear walls was comparable to that of cast-in-place shear walls, with the yield loads of each specimen being satisfactory. Despite these advantages, the concealed nature of grouting and the lengthy curing time necessitate recent interests to develop dry connections. Innovative dry connection methods introduced by Li et al. [13], Fu et al. [14], and Ding et al. [15] demonstrated promising load-bearing capabilities, with Ding et al.'s detachable DfD (design for deconstruction) connection being particularly noteworthy. In this process, machine learning has also been applied in relevant research fields [16].

Various forms of PC shear walls are continuously emerging, and researchers have conducted low-cycle reversed loading tests to confirm their feasibility. However, during their service life, shear walls might suffer various extreme loads, such as landslides, vehicular collisions, or gas explosions that could lead to progressive collapse like the Ronan Point apartment accident. Unlike the effects of compression, flexural, and torsion under static loads, steel rebars and concrete materials exhibit significant strain-rate effects under dynamic loads [17–20], leading to different failure modes, plastic deformations, and even structural collapse that might not happen under static conditions. Hence, the structural resistance of concrete structures under dynamic loads attracted substantial research focus: Zineddin et al. [21], Sadraie

* Corresponding author.
E-mail address: sunjingming@hnu.edu.cn (J.-M. Sun).

https://doi.org/10.1016/j.engstruct.2024.118748
Received 16 March 2024; Received in revised form 8 July 2024; Accepted 5 August 2024
Available online 9 August 2024

et al. [22] and Sengel et al. [23] carried out drop hammer tests of plates. Researchers [24–26] have performed systematic research on the impact behavior of reinforced concrete beams considering the importance of beams as the main horizontal members. In terms of vertical members, some studies on columns are also reported [27–30]. Researchers found that the axial compression ratio was favorable for impact resistance within certain ranges in which the critical value was determined as 0.24 [28,29]. In addition, the resistance of beam-column joints under impact load has also been studied [31]. However, little attentions were paid on shear walls compared with above-mentioned members. Wang et al. [32] conducted eight large-scale rigid projectile impact tests on RC shear walls, and the results indicated that walls with U-shaped transverse steel exhibited superior performance than traditional hoop reinforcement walls in terms of perforation capacity. Shi et al. [33] studied the impact resistance of civil air defense engineering shear wall. It was shown that when the impact height increased from 0.4 m to 2.5 m, the impact failure mode tended to be localized, and the horizontal displacement in the middle of the wall span increased. Shi [34] studied the difference between PC shear wall and cast-in-situ shear wall with grouted sleeve connection under impact load. The experimental results suggested that the peak value of impact force is sensitive to the contact stiffness. When the impact velocity is constant, the change in impact mass has no obvious influence on the peak value of impact time history curve, but it did affect the maximum horizontal displacement of reinforced concrete wall slab. However, in those tests, the axial stress states of walls or edge members is not considered, which might lead to unrealistic performance and inaccurate results.

Research in structural impact resistance has primarily been directed at cast-in-situ concrete structures, with scant attention to PC structures' impact resistance capabilities. The discontinuity of rebar in PC structures raises concerns about the adequacy of force transfer. Although consensuses have been achieved that PC shear walls can provide sufficient in-plane bearing capacity with proper design and construction, the behavior of assembly joints under impact loads remains largely unexplored and potentially vulnerable, especially when constant axial compression forces are applied. Thus, it is essential to investigate the impact resistance of PC shear walls with various connections for the safety and robustness considerations. Moreover, consistently applying axial loads during tests, particularly for shear walls subjected to high axial compression ratios, presents significant challenges.

In this study, pendulum impact tests were performed on three PC and one RC specimens, with different connection types at the PC shear wall-footing interface as the variables. Utilizing a pendulum impact apparatus, constant axial loads were applied atop the shear wall imitating actual axial compression ratios in real-world structures. The analysis covered impact resistance aspects such as failure modes, crack progression, impact force-time dynamics, axial force-vertical displacement correlations, deformation patterns, material strains, energy dissipation, and inertia forces. Moreover, the study juxtaposed the impact force differences between PC shear walls and corresponding PC columns, proposing a novel method to assess the impact resistance of wall panels.

2. Experimental program

2.1. Specimens design

Three PC shear wall specimens with different connection forms (the grouted sleeve connection, the grouted corrugated metallic ducts connection, and the bolt connection) and one cast-in-situ shear wall specimen were designed for pendulum impact experiment. All specimens were designed with identical geometry and reinforcement ratio according to GB50010–2010 [35], as shown in Table 1. The dimensions of the shear walls in this experiment were referenced from literature [36]. The prototype was designed in Shanghai, China, and comprised a 38.6-meter tall, 13-story PC shear wall structure, with original dimensions of 1800 mm × 200 mm× 2750 mm. A scale ratio of 3:4 was selected based on dimension specifications of the pendulum impact apparatus with according adjustments to fit specimens into the apparatus. The width of specimens was 1300 mm, the height was 2400 mm, and the thickness was 150 mm, with the 200 mm edge members. The foundation of the specimens was secured to rigid floor slots by eight anchor rods and bolts passing through the specimens and slots.

Table 1
Summary of specimen details.

Specimens	Concrete strength	Shear wall reinforcement	Edge members reinforcement	Connectors
RC	C35	Vertical : 6T12(0.262 %) Transverse : T8 @ 200(0.251 %)	Longitudinal reinforcement : 4T16 Transverse reinforcement : T6 @ 200	None
PC1				Grouted sleeve
PC2				Metallic ducts
PC3				Steel box connectors

During the construction of PC1 and PC2, the upper cap beam and shear walls, including edge members, were monolithically poured, and the foundation beams were poured separately prior to the assembly. PC3 required high precision in hole locations, therefore the foundation beam was constructed first. The vertical distributed bars were then bound and connected to steel box connectors, and the shear wall, the edge members, and the upper cap beam were poured. The assembly process of PC3 complied with the requirements of GBT51231–2016 [37] and JGJ1–2014 [38]. A 20 mm thick high-strength grout layer was set at the joints of PC1~PC3. The specimen dimensions and reinforcement layouts are illustrated in Fig. 1.

In specimen PC1, longitudinal rebars of edge members and vertical distributed rebars of walls were connected to the foundation using grouted sleeves that was made of ductile iron with two different diameters (GTZQ4–16A and GTZQ4–12A), as illustrated in Fig. 2(a). The anchorage length of rebars at both grouted sleeves was 8*d*, where *d* refers to the diameter of the connected rebars, as depicted in Fig. 3(a). The sleeves were grouted with TT-100 high-strength grouting material, and the spacing between the horizontal distributed rebars within the sleeve's height was 100 mm.

In specimen PC2, the anchorage length within the pre-embedded corrugated pipes were determined as 495 mm and 650 mm in accordance with GBT51231–2016 [37], respectively. The 35 mm diameter galvanized corrugated pipes were bended at one end to facilitate grouting, as shown in Fig. 2(b) and Fig. 3(b). The grouting material selected was self-compacting and aggregate-free cementitious grout material (CGM) high-strength grout in case of blockages.

In specimen PC3, vertical distribution bars were connected by steel box connectors, while the longitudinal rebars of edge members were tied through splicing, as illustrated in Fig. 2(c). The steel box connector was designed based on T/CECS 809–2021 [39]. This connector consisted of an upper steel bar extending into the wall and a steel box as depicted in Fig. 3(c), where the upper steel bar passing through the top of the connector and were welded in place.

2.2. Material properties

The properties of the steel, concrete, and cement-based materials used in the experiments are detailed in Table 2 and Table 3. For each type of rebar, three 500 mm long samples were tested based on GB/T228.1–2021 [40], and their yield strength and ultimate strength were measured by an electro-hydraulic servo testing machine. The concrete compressive strength was measured on six 150-mm cubic specimens and three D150 × 300 mm cylindrical specimens for each specimen in accordance with GB/T50107–2010 [41]. Three 40 × 40 × 160 mm specimens were prepared for grouting materials in each specimen, in which flexural tests were conducted prior to compressive tests. As for the grout layer, three 70.7 × 70.7 × 70.7 mm specimens were prepared for

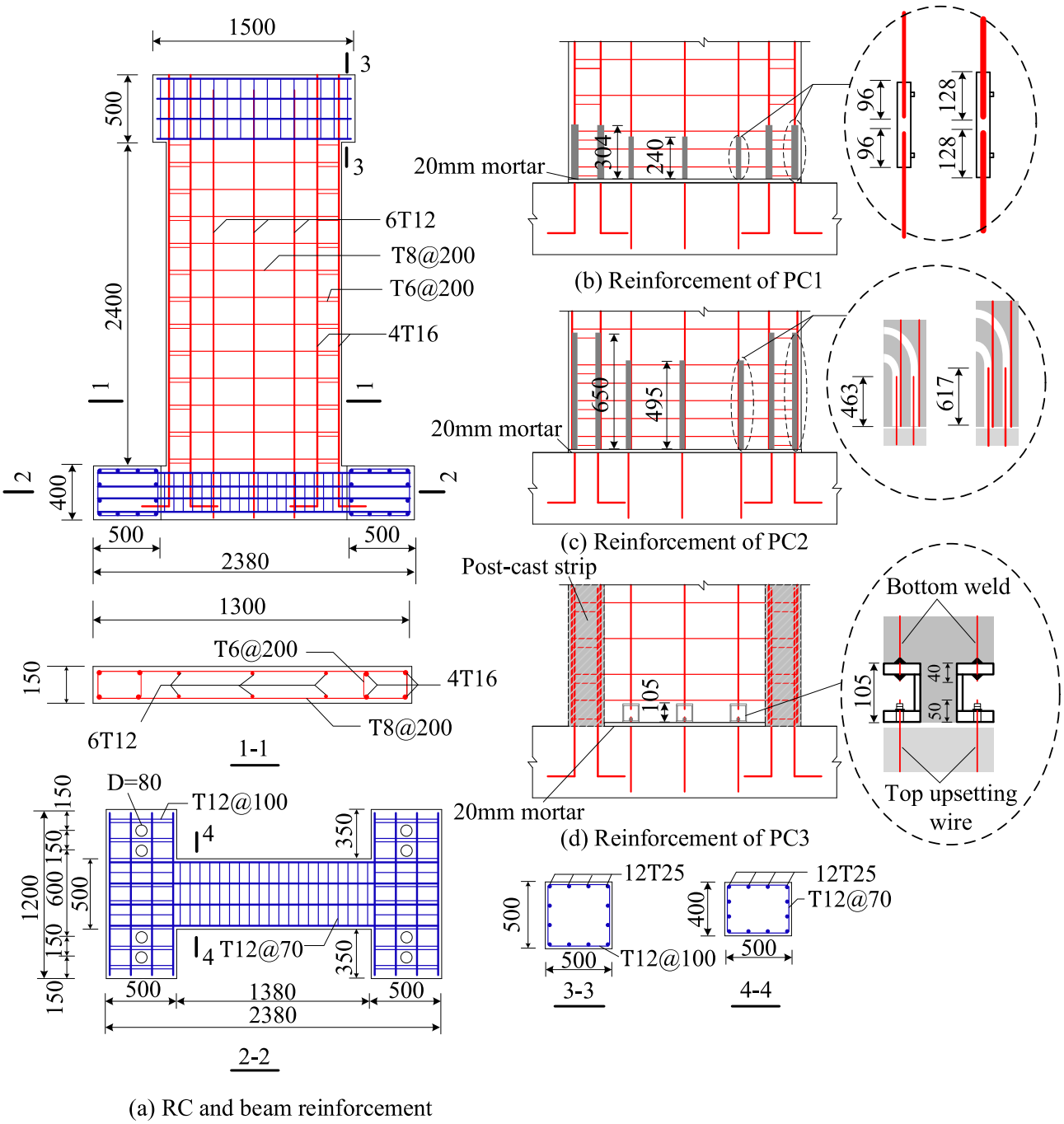

Fig. 1. Dimensions and reinforcement layouts of specimens (unit: mm).

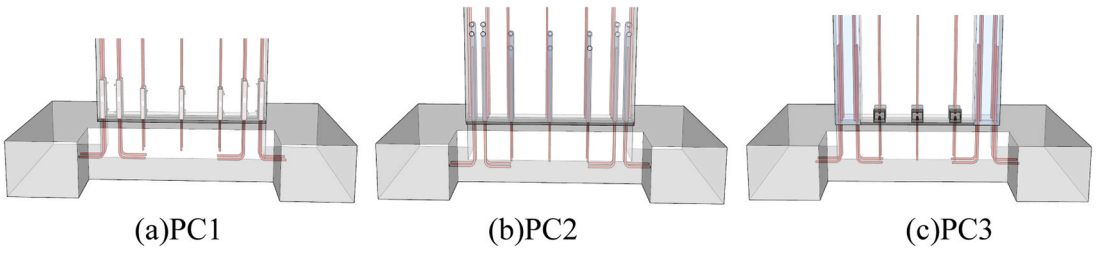

Fig. 2. Details of shear wall-footing connection.

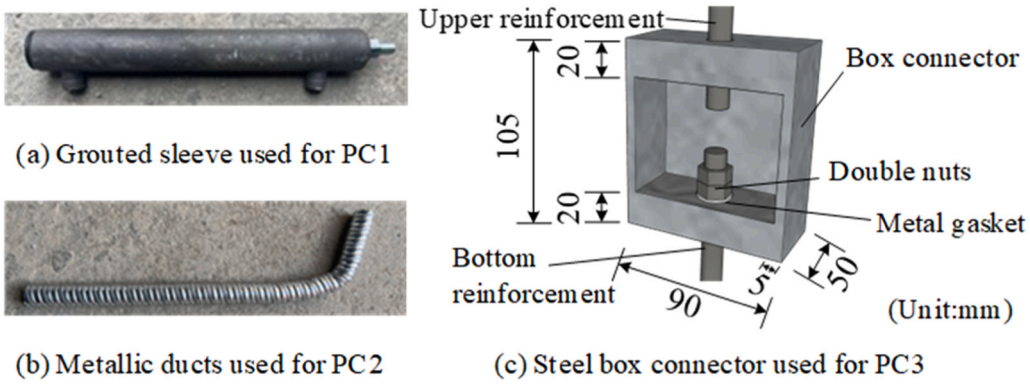

Fig. 3. Connector used for PC.

Table 2
Material properties of reinforcement and concrete.

Material	Strength grade	Yield Strength (MPa)	Ultimate Strength (MPa)
Reinforcement	HRB400	468	623
Concrete	C35	-	33.4
Connector steel	Q235	235	370 −500

Table 3
Material properties of cement-based materials.

Test block type	Flexural strength (MPa)	Compressive strength (MPa)	Specific location
TT−100 Sleeve grouting	14.5	90.4	PC1 (Grouted sleeves)
CGM High strength grout	10.1	117.4	PC2 (Metallic ducts)
Grouted layer material	-	73.2	PC1/PC2/PC3 (Grout layer)

each specimen. The sampling and testing of the above cement-based materials followed the GB/T17671–2021 [42] and JGJ/T70–2009 [43].

2.3. Test setup and instrumentation

Fig. 4 illustrates the adopted pendulum impact apparatus, which has been described in detail and proven reliable in previous studies [29,30]. The apparatus mainly composed by a reaction frame, a pendulum applying impact loading, and a loading frame system exerting axial force

Table 4
Experimental conditions.

Specimens	Axial compression ratio	Impact velocity (m/s)	Impact mass (kg)
RC/PC1/PC2/ PC3	0.13	5.77	2167

through the lever principle. Loading parameters were identical for all specimens and are listed in Table 4. The axial compression ratio determined as $\mu = N/f_cA$, where N and A were the axial compression force and cross-sectional region respectively, and f_c was the average measured compressive strength of the shear wall concrete prism specimen. Consequently, the ratio is determined as 0.13, which is considered the optimal adaptation to the test conditions and equipment capabilities. The impact velocity and mass were determined based on the approach outlined in literature [44,45]:

$$\frac{m_2 v_{ib}^2}{2} - E_R + \left(m_1 + m_2\right) g\delta_{\max} = W \tag{1}$$

$$E_R = \frac{m_1 m_2}{2(m_1 + m_2)} v_{ib}^2 \tag{2}$$

where m_1 is the equivalent mass of the RC shear wall, m_2, v_{ib} are the mass and velocity of the pendulum, respectively, E_R is the energy loss during the impact process, δ_{max} is the maximum mid-span displacement of the RC shear wall; and W is the deformation energy corresponding to $\delta_{\max}$ under static loading, calculated according to the finite element method. Based on the research findings of Kishi et al. [46], $\delta_{\max}$ was set to 1.4 %

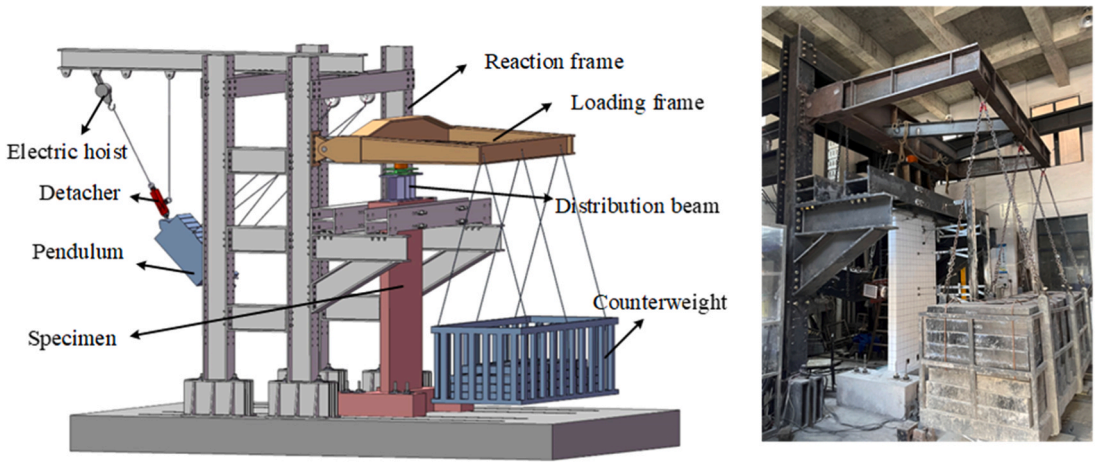

Fig. 4. Test setup and loading method.

of the wall height and was considered as a performance index of the impact resistance of shear walls.

To obtain the dynamic response of specimens under impact loading, recorded data were as followed: (1) displacement at measurement points on the wall and edge members; (2) impact force at the pendulum head and axial force at the top of the specimen; (3) strain of rebars at the joints and near the impact point; (4) strain of the concrete at the bottom of the wall; (5) acceleration at select measurement points; and (6) High-speed images during the impact process.

The detailed locations of the measurement points are illustrated in Fig. 5. The displacements were measured (marked in red) on the back side of impact, where W5 and W8 denoted vertical displacement, and the others denoted lateral displacement. Two displacement transducers, W2 and W3, measured the lateral displacements of the impact point guaranteeing the data redundancy due to possible transducer failures during the impact. Accelerometers (marked in purple) were placed on the same side as the impact and all oriented in the same direction as the impact. Concrete and rebar strain gauges were positioned on both sides but are only shown on the impact-facing side in the figure.

All data except strain were collected using Advantech data acquisition systems (PCI-1714UL) at a sampling frequency of 200 kHz. Strain data were obtained using TMR-211 and TMR-311 at a sampling frequency of 1000 Hz. The models of both the impact force sensor and the axial force sensor were KCE-2MNA and the measuring range was 0–2000 kN. The maximum acceleration that the accelerometer sensor could measure was 10,000 g. To investigate the crack propagation process, one high-speed camera (Optronis: CP70–1HS-M-1900) was set up to capture high-frequency images of the entire specimen at a frequency of 2000 Hz.

To facilitate the research on the overall deformation and the failure mode of shear walls, the pendulum had an arc-shaped head, and a round steel plate (D400 ×50 mm, made of Q345 steel material) was closely adhered by epoxy adhesive to the specimen in front of the pendulum to prevent unfavorable localized damage on the wall. After impact, no apparent perforation or indentation was observed on the round steel plate and the specimen, indicating that the plate expectedly dispersed the impact force and prevented the localized damage.

3. Experimental results

3.1. Failure modes

Fig. 6 illustrates the failure modes of each specimen on the back side. Among the specimens, the back side of the RC specimen exhibited radially distributed cracks in which a significant critical crack appeared at the wall's mid-height impact point. In addition, numerous fine cracks developed around the critical crack and predominantly extended towards the wall's edges.

The PC1 specimen resembled its RC counterpart in terms of the distribution of horizontal and vertical cracks yet differed notably in the quantity and form of diagonal cracks. A greater number of diagonal radial cracks was observed, suggesting stress concentration in the connections of prefabricated components as a likely cause for this variation. Additionally, horizontal cracks appeared at the sleeve connection area of the wall section, possibly owing to the bond slip of rebars within the sleeve.

The PC2 specimen demonstrated two predominant failure modes: initially, it showed horizontal critical cracks and then scabbing failure, resembling modes reported on reinforced concrete slabs under impact loads [47]. This scabbing was especially marked in the wall's upper-middle section, characterized by extensive concrete spalling and localized damage. This phenomenon is likely due to inadequate force transmission at the bottom rebars' indirect lap splice. The presence of cracks in the grout layer, coupled with axial compression, limited crack propagation and impact energy absorption at the base. Furthermore, the bottom's denser horizontal reinforcement increased structural stiffness, predisposing the upper region with less stiffness to failure.

The PC3 specimen exhibited horizontal critical cracks on the back side like the PC1 specimen with slightly greater magnitude. The PC3 specimen differs from the other two PC specimens because the edge members and wall were casted step-by-step, so vertical cracks were observed at the concrete interface, indicating potential minor slippage between new and old concrete segments. Notably, previous experiments of PC columns [30] showed significant damage more severe than the RC counterpart at the bottom bolt connection of specimens. However, damage on the shear wall specimens with steel box connectors was marginally higher than that of the RC specimen in this experiment, suggesting that edge members substantially enhances the lateral stiffness of the shear wall.

After impact, observations revealed that specimens primarily failed due to flexural stresses, attributed to the bending deformations exceeding their maximum rotational capacity under out-of-plane impact loads. Notably, the emergence of distinct critical cracks or plastic hinge zones was evident, especially on the back sides where the adjacent steel rebars yielded. These cracks, radiating outward from the impact zone, alongside a marginally higher occurrence of horizontal over vertical cracks due to fixed top and bottom constraints, resembled the crack patterns observed in one-way slabs during flexural failure. This suggests a localized effect caused by the shock wave propagation within the wall. Compared to the PC specimens, the RC specimen exhibited significantly fewer cracks, indicating a superior overall stiffness.

Fig. 7 and Fig. 8 exhibit the failure modes on the impact and side faces of the specimens characterizing by different crack distribution patterns due to varying boundary conditions between RC and PC specimens, yet similar flexural failure modes on the side faces (edge members). Cracks on the RC specimen mainly developed at the top and

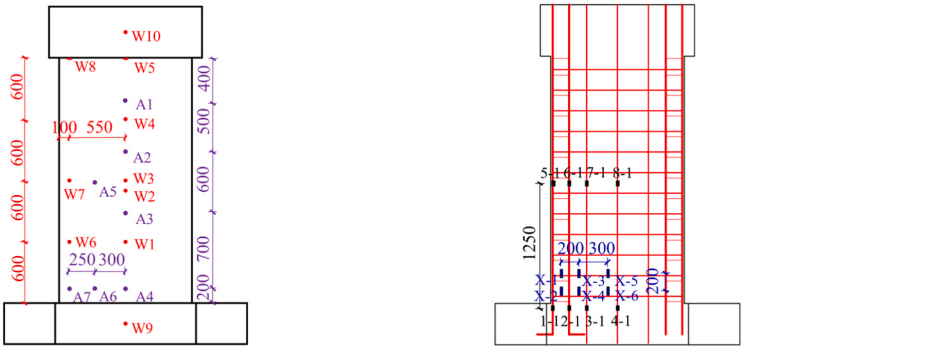

(a) Displacement transducers and accelerometers (b) Reinforcement and concrete strain gauges

Fig. 5. Instrument arrangement.

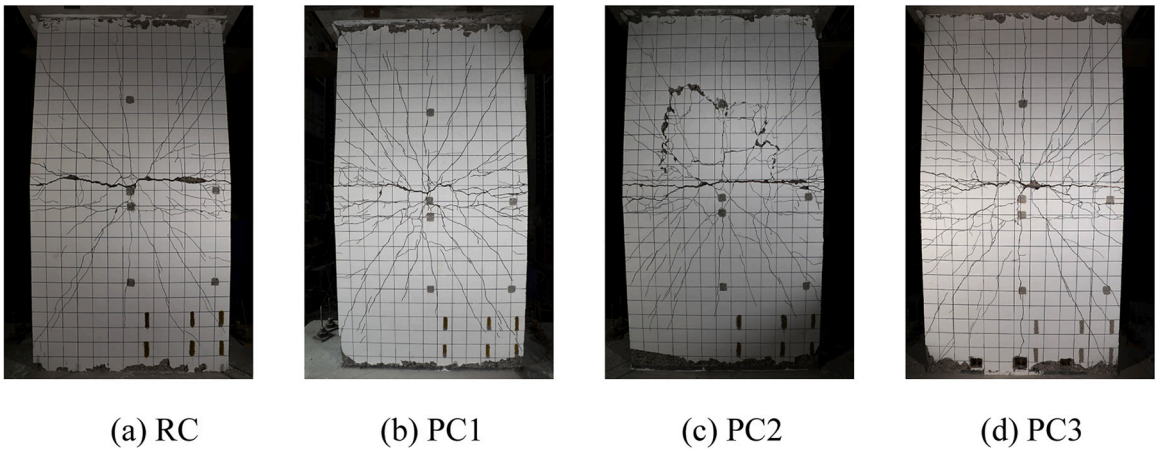

Fig. 6. Failure modes of shear walls on the back side.

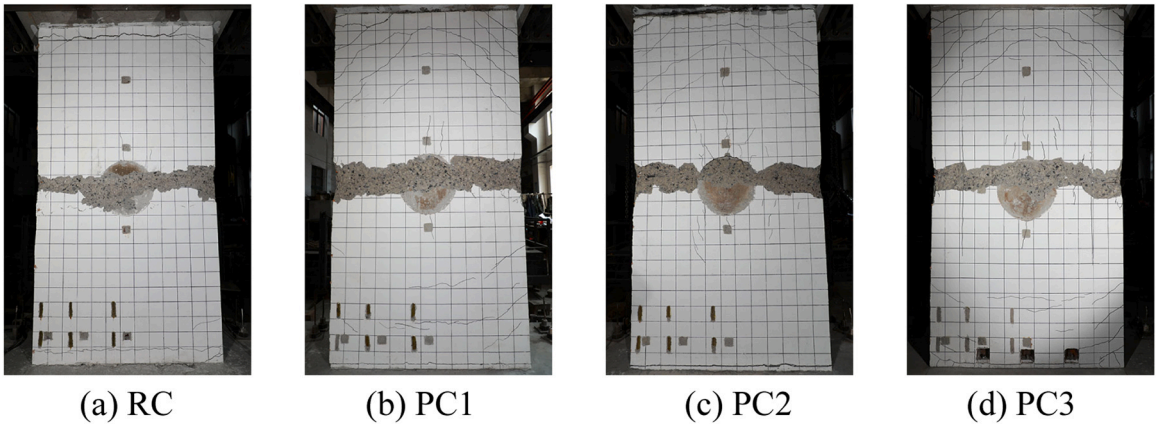

Fig. 7. Failure modes of shear walls on the impact-facing side.

bottom beams' contraflexure points. The PC1 specimen featured with circular cracks around the impact center on the impact-facing surface. For PC1 and PC2, bottom grout layer cracks absorbed most impact energy, minimizing bottom cracks. Conversely, the PC3 specimen experienced severe detachment between the steel box connection and the grout with a notable number of cracks in edge members, indicating higher energy absorption during impact.

3.2. Crack propagation

The high-speed camera captured the crack propagation processes of every specimen, as illustrated in Fig. 9. Initially, the crack development in both RC and PC specimens are similar. Then PC specimens consistently exhibited more cracks compared to the RC counterpart, highlighting the structural disparities caused by the prefabrication.

At the 3 ms, both RC and PC1 specimens showed symmetric crack patterns, yet PC1 exhibited more cracks. The PC2 specimen was characterized by a singular 45° diagonal crack wider than others, contrasting with PC3's irregular crack distribution. By 10 ms, horizontal cracks in PC specimens widened beyond those in the RC specimen, with PC1 displaying a markedly higher number of cracks. PC2 had fewer cracks above the impact point, predominantly due to the wide 45° diagonal crack, while the crack distribution in other specimens was more even across the impact point. By 25 ms, the wide diagonal crack in PC2 further propagated and initiated scabbing, with PC1 and PC3 exhibiting significantly more cracks than the RC and PC2 specimens. By 80 ms, extensive scabbing and through-wall cracks developed in PC2, illustrating diverse impact resistances and damage patterns among the specimens.

3.3. The history curve of impact force and displacement of the impact point

Fig. 10 illustrates the impact force time history curves of each specimen in which a consistent pattern was identified with a brief, high-peak temporary wave followed by a longer, lower-peak main wave. The impact force initially spikes sharply, then quickly drops near zero before a second, smaller peak emerges, eventually fading as the wall undergoes vibrations. This secondary peak might be caused by pendulum rebounds after initial impact contact, so its magnitude was much smaller because a portion of energy has been absorbed or dissipated by the wall.

To ensure a comprehensive analysis, various impact force-related parameters were defined in the study: F_p denotes the peak impact force, representing the maximum force recorded by the sensor at the hammer head, largely dependent on contact stiffness and impact velocity [48,49]. t_p is the time to peak impact force evaluating the rate of force escalating to the peak, and it is also an indicative of the specimen's stiffness; $F_{ave,p}$ is the average force during the plateau phase of the impact force-time curve, providing insights into the specimen's overall damage level; and t_d represents the impact force duration, spanning from the pendulum's contact with the specimen until their separation. Additionally, the impulse I_p, which quantifies the cumulative impact of force over time, was employed to calculate the overall average impact force F_{ave} for each specimen, detailed in Table 5 and exemplified through the RC specimen in Fig. 11 for subsequent discussion.

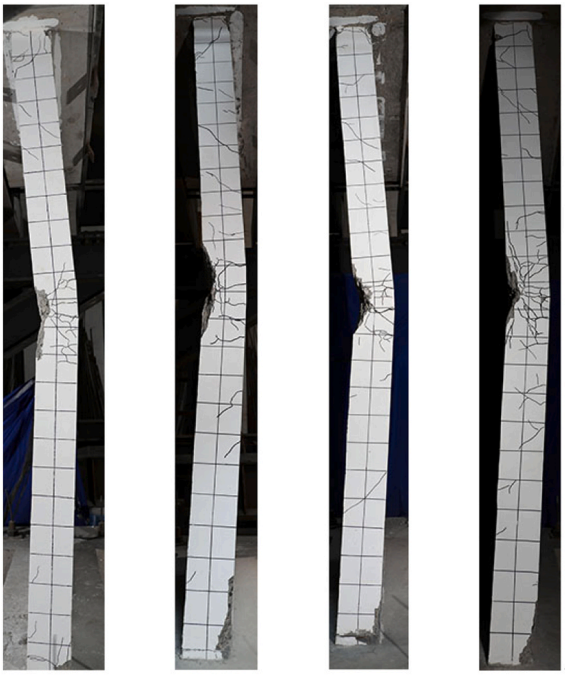

Fig. 8. Failure mode of specimen side face (edge members).

$$I_p = \int_{t_1}^{t_2} F dt \tag{3}$$

$$F_{ave} = \frac{I_p}{t_d} \tag{4}$$

$$t_d = t_2 - t_1 \tag{5}$$

where t_1 was the start time of impact, t_2 was the end time of impact, and F was the impact force.

Fig. 10 reveals distinct differences in the peak impact forces and the time to peak among the specimens. The RC specimen, with its peak force reaching 1582 kN in just 1.20 ms, underscores its superior stiffness compared to the PC specimens. The PC1 and PC3 specimens demonstrated comparable while slightly lower stiffness than the RC counterpart. The PC2 specimen showed the lowest stiffness among them. The analysis also illustrated that the average impact forces for PC1 and PC2 were marginally higher than those for the RC and PC3 specimens, suggesting that delayed scab formation had a minor influence on these measures. Further, the PC2 specimen exhibited a longer impact duration and greater cumulative impact force highlighted by its reduced stiffness. Moreover, the comparison of average impact forces suggested a nuanced relationship among the specimens, with the PC1 and PC3 specimens showing variations indicative of their differing energy dissipation and ductility characteristics, as highlighted by a previous study [30].

To compare the response characteristics of different structural forms under similar impact conditions, the impact force time history curves obtained in this test were normalized with the impact force time history curves of PC columns in the literature [30], which showed that semi-rigid boundary conditions of PC columns decreased the column damage, but the lateral deformation increased, indicating relatively low impact resistance. The peak normalization method was adopted, with the vertical axis representing the normalized impact force F/F_p (F represented the impact force at each moment, F_p represented the peak impact force), and the horizontal axis representing time. Fig. 12 shows the normalized impact force time history curves for each specimen. It can be seen that the impact force time history curves for the shear wall specimens and column specimens with different connection methods had similar trends, with distinct peak, plateau, and unloading stages. However, the main differences between column specimens and shear wall specimens are the duration of the peak stage and the duration of the impact force. Specifically, in terms of the duration of the peak stage, the decrease rate of impact force for column specimens after reaching the peak was significantly faster than that for shear wall specimens, with a difference in duration of about 55%, indicating similar properties. This may be attributed to the rapid decrease in stiffness of column specimens after the impact force reached its peak, while the overall stiffness of shear wall specimens is relatively unaffected due to edge members. As for the duration of the impact force, column specimens were significantly longer than shear wall specimens, especially in the unloading stage where the difference was apparent. This might be explained by higher stiffness of shear wall specimens resulting in faster rebound of the pendulum and earlier separation of the hammer head, leading to faster energy dissipation. The time differences are also considerable between column specimens and shear wall specimens with different connection forms, reflecting the differences in application between different connection forms in column specimens and shear wall specimens. Although the times at which the second peak impact force occurred vary, except for the bolt connection shear wall specimens and column specimens, the second peak impact force of other connection forms was approximately 20% to 30% of the first peak, indicating that the second peak impact force proportion of bolt connection column specimens exceeded 40%, possibly due to more severe shear failure at the bottom.

Fig. 13 presents the displacement history curves including both loading and unloading phases at the impact points for each specimen, and peak displacement D_p and residual displacement D_r details are listed in Table 5. Lateral displacement increases to its peak in the loading phase, with the RC, PC1, and PC3 specimens showing similar patterns, whereas the PC2 displays a markedly higher peak displacement, suggesting the lowest initial stiffness. Then the displacement reduced to the residual level in the unloading phase, and PC2 specimen also exhibited the largest residual displacement indicating its distinct behavior compared to other specimens.

3.4. Axial force and vertical displacement

Fig. 14 illustrates the axial force and vertical displacement time history curves for each specimen. It is worth noting that initial variations were affected by sensor setup and measurement inaccuracies. Despite the uniform axial compression ratio, initial axial forces slightly differed. Vertical displacements at the center of walls and edge members, denoted as W5 and W8, started when axial force reaching 830 kN, in which the positive values signify downward movement. Initially, the surged axial force mirrors peak vertical displacement and indicates an arching effect. Particularly for PC2, a marked decrease in post-damage stiffness was observed as axial force dipped below its initial value, followed by stabilizing fluctuations due to vertical vibrations. Displacements of edge members are similar to the center of wall but were less pronounced, and this might be attributed to enhanced stiffness from a higher reinforcement ratio.

3.5. Deformation curve

Fig. 15 shows the displacement curves between the edge members and the walls for each specimen, which are roughly consistent at the same height. The upper displacements in every specimen, consistent with previous research results, were generally greater than the lower displacements, suggesting the phenomenon might originate from the higher stiffness of the bottom boundary constraints rather than the axial force or the action of the edge members. The specimens reached peak displacement at 0.04 or 0.05 s after impact, followed by rebound due to the release of elastic potential energy, and resulting in a reduction in displacement to residual deformation. Particularly, the PC2 specimen

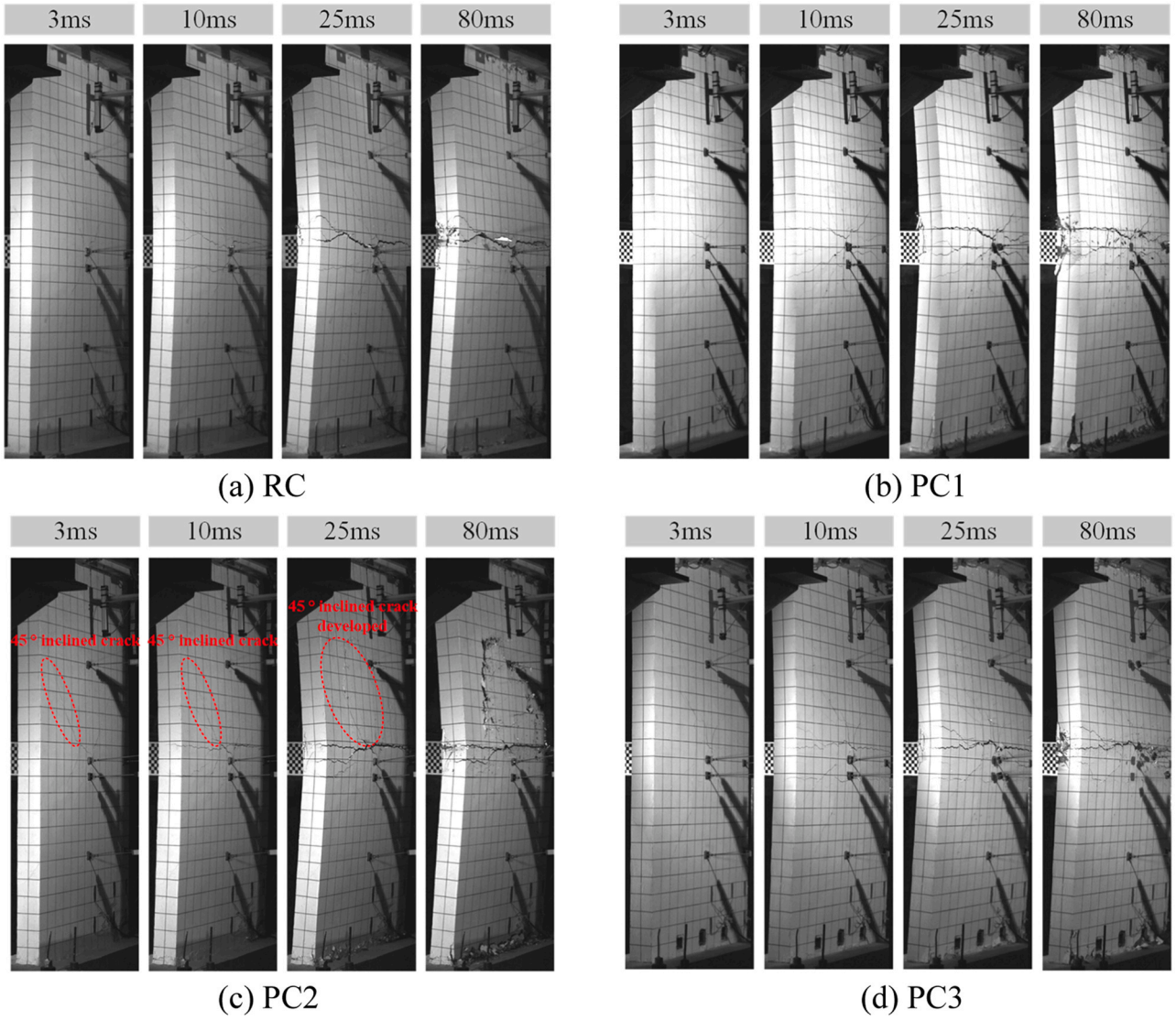

Fig. 9. Crack propagation.

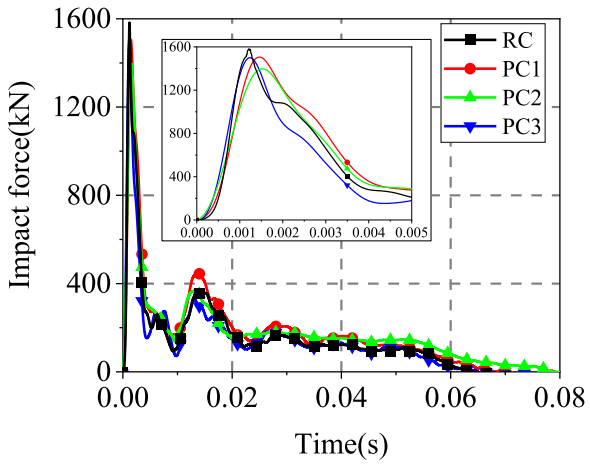

Fig. 10. Impact force time history curves.

exhibited the largest peak and residual displacements, indicating its lowest overall stiffness. Compared to previous experiments on shear walls without axial force and edge members, specimens in this study reached residual deformation by shorter time, implying that the presence of axial force and edge members increased the overall stiffness of the shear walls and shorten the duration of deformation.

3.6. Concrete and steel strains

Due to the significant impact energy during the experiment, some strain gauges were damaged or produced incomplete data. Therefore, selected data from intact strain gauges are presented in this section. Fig. 16 presents the strain-time curves of the concrete at the bottom of the impact-facing side. It can be observed that the micro strain peak of the RC specimen ($\mu\varepsilon$ =458) was much lower than that of the PC1 specimen ($\mu\varepsilon$ =2800), PC2 specimen ($\mu\varepsilon$=1103), and PC3 specimen ($\mu\varepsilon$ =2680), revealing that the extent of concrete damage at the bottom of the impact-facing side was lighter for the RC shear wall. This phenomenon might have been related to the formation of significant horizontal cracks at the top of the RC specimen, which could have alleviated the stress state at the bottom of the concrete, thereby reducing the damage.

Fig. 17 displays the strain-time curves of the concrete at the bottom of the back side. The observed strain patterns are consistent with the results shown in Fig. 16. In all specimens, the bottom concrete of the RC specimen suffered relatively minor damage for its strain was the smallest. All specimens exhibited compressive strain peaks under the

Table 5
Experimental results.

Specimen	F_p (kN)	I_p (N·s)	F_{ave} (kN)	$F_{ave,p}$ (kN)	t_d (ms)	F_p/F_{ave}	t_p (ms)	D_p (mm)	D_r (mm)
RC	1582	11.45×10^3	177.5	121.8	64.5	8.9	1.20	92	70
PC1	1506	13.61×10^3	202.8	152.1	67.1	7.4	1.47	91	69
PC2	1396	13.78×10^3	177.1	156.6	77.8	7.9	1.54	103	86
PC3	1500	10.74×10^3	167.6	124.8	64.1	8.9	1.24	92	65

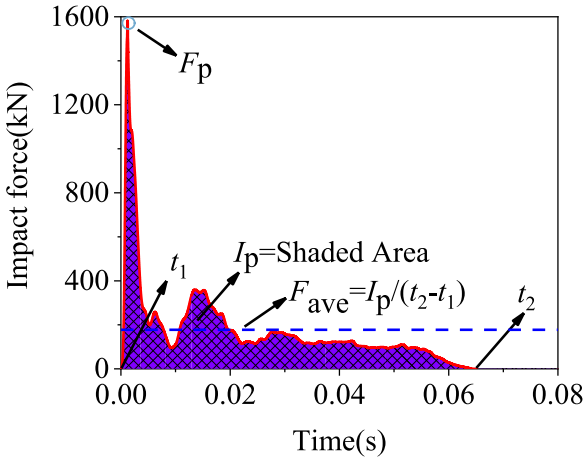

Fig. 11. Characteristic curve of RC specimen.

impact loads, after which these micro strain values stabilized within the range of 0–1000.

Fig. 18 illustrates the strain history of rebars on the impact-facing side. It is observed that all rebars reached yielding states in both the RC and PC1 specimens. In the PC2 specimen, only some longitudinal rebars (labeled as 7–1 and 8–1) remained elastic that might be ascribed to the detachment of the scab formed by the outer concrete and leading to significant energy dissipation. Similarly, in the PC3 specimen, only some longitudinal rebars (labeled as 6–1 and 7–1) did not yield, which might be related to the consumption of the preload force of the bottom bolts. It is noteworthy that in the PC2 specimen, the edge members connecting rebars (labeled as 1–1 and 2–1) exhibited a strain plateau for about 0.026 s and 0.02 s possibly reflecting the process of scab formation. Further observation revealed that the strain of connecting rebar 2–1 significantly increased to approximately 3.3 times at 0.025 s, coinciding with the time of scab formation as shown in Fig. 18(c). It indicates that the scab formation led to a significant increase in the strain of the main stress-bearing rebars due to substantial concrete spalling.

Fig. 19 illustrates the strain time history curves of the rebars on the back side. It can be seen from the figure that the rebars in both the RC and PC1 specimens reached yield states like the results in Fig. 18, so the stress conditions are similar for the main rebars in the RC and PC1 specimens. However, in PC2 and PC3 specimens, some rebars (labeled as 1–2 and 2–2 in PC2 and 1–2, 2–2, 3–2 and 4–2 in PC3) did not yield, and the peak strain of the rebars connected with the foundation beam (labeled as 1–2, 2–2, 3–2, and 4–2 in PC2 and PC3) was significantly lower than that of RC and PC1 specimens, indicating deficiencies in the transfer efficiency of these two connection methods. Furthermore, significant differences exist on the strain peaks of the impact-facing side rebars (labeled as 1–1, 2–1, 3–1, and 4–1) and rebars near the back side (labeled as 1–2, 2–2, 3–2, and 4–2) in the PC2 and PC3 specimens by the comparison in Fig. 18 which indicates significant differences in stress between the two rows of rebars. Limitations in the energy dissipation are identified for the double-layer bidirectional reinforced framework.

4. Analysis and discussion

4.1. Energy dissipation

The force-displacement curves are depicted in Fig. 20. The initial waveform of the impact force (temporary wave) predominantly influenced the overall deformation of the wall, with the main waveform approximately exhibiting a triangular distribution. After reaching the peak displacement, all specimens experienced a rebound phenomenon related to the horizontal inertial effect. In the early stages of the impact, similar patterns of force-displacement curves can be observed among the specimens. However, once the impact force reached its peak, the curve of the PC2 specimen exhibited a significantly faster descent rate compared to other specimens, and this might because the PC2 specimen suffered more severe local damage.

By integrating the force-displacement curves, the deformation energy E_d of each specimen could be obtained. The deformation energies of the specimens were 34.076 kJ, 32.137 kJ, 28.841 kJ, and 25.195 kJ, respectively. The energy dissipation ratio was defined as follows:

$$\lambda = \frac{E_d}{E_k} \tag{6}$$

Fig. 21 illustrates the energy dissipation ratio that reflect the proportion of energy dissipated through deformation to the total input energy. The energy dissipation ratio of the RC specimen is higher than that of each PC specimen, indicating that the RC specimen primarily dissipated impact energy through the bending deformation of the wall. The energy dissipation ratio of the RC specimen (0.944) and PC1 specimen (0.890) are similar, significantly higher than that of the PC2 specimen (0.799) and PC3 specimen (0.698). This suggests that the energy dissipation mechanism of the PC1 specimen is like that of the RC specimen, i.e., energy are primarily dissipated by deformation. It also indicates that the grouted sleeve connection PC shear wall could be considered emulative to cast-in-situ members. The lower energy dissipation ratio of the PC2 specimen was due to severe local damage, with energy dissipated in the form of concrete spalling, resulting in less energy dissipated through deformation. On the other hand, the PC3 specimen dissipated less energy through deformation due to the consumption of pre-tension force in the bottom bolts.

4.2. Analysis of inertial force

During the early stage of impact, the support reaction forces could be neglected as stress waves have not reach the upper and lower boundaries of specimens. At this point, the impact force was primarily resisted by inertia force. Utilizing the mass discrete method, the inertial forces of each mass point can be calculated separately, where the mass blocks were divided using the centers of adjacent accelerometer sensors as boundaries. The simplified computational model is illustrated in Fig. 22. By summing up the inertial forces of these mass points, the overall lateral inertial force of the shear wall can be obtained. Therefore, the horizontal overall inertia force of each specimen was calculated using the following equation, which has been applied in relevant literature concerning columns [29,50].

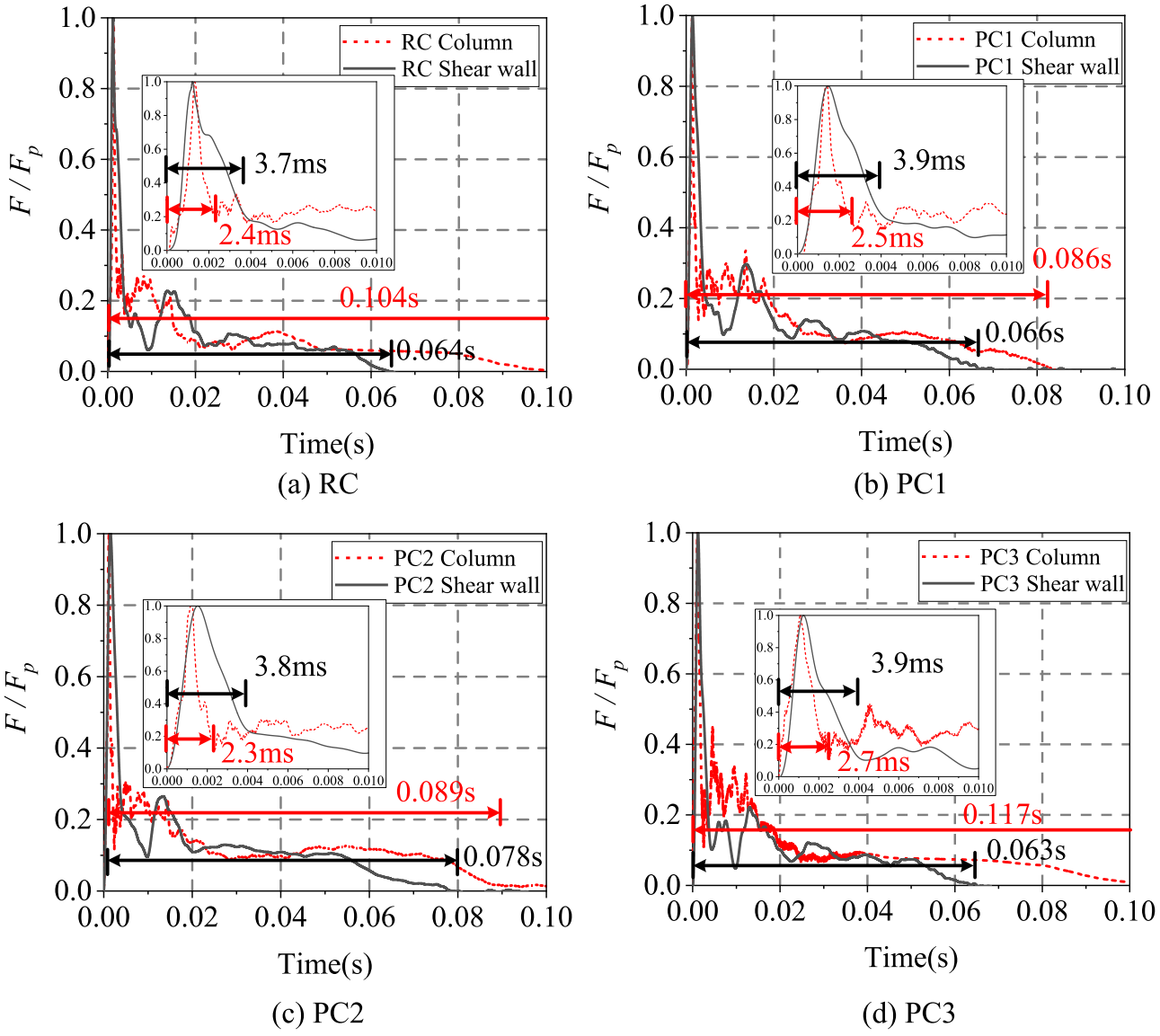

Fig. 12. Comparison of impact force between shear wall and column.

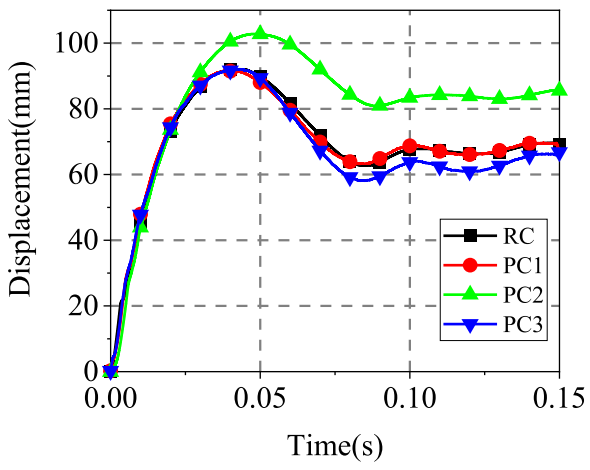

Fig. 13. The displacement-time curves at the impact center.

$$I_H = -\int_0^h \overline{m} a_H\left(x,t\right)dx = -\overline{m}\left[\frac{13}{20}\left(A_1(t)+A_3(t)\right)+\frac{11}{20}\left(A_2(t)+A_4(t)\right)\right] \tag{7}$$

where I_H represents the horizontal overall inertial force, which is the summation of the inertial forces of individual mass points, representing the overall magnitude of the inertial force of the shear wall specimen. h represents the height of the specimen, $\overline{m}$represents the linear density of the wall, $a_H(x,t)$ represents the acceleration at different positions.

In Fig. 23, the calculated inertia force is compared with the measured impact force. It is observed that the peak values of the horizontal overall inertia forces for each specimen are quite close to the measured impact force, with their ratios ranging from 0.86 to 0.93. This is consistent with the results in reference [29], further demonstrating that during the early stage of impact, the impact force is primarily resisted by horizontal inertia forces. The peak values of the inertia forces for all specimens occurred between 0.7 ms and 0.9 ms, while the peak values of the impact forces occurred between 1.2 ms and 1.6 ms. This indicates that inertia forces reach their peak values before the impact forces during the impact process. The inertia force-time curves for each specimen show

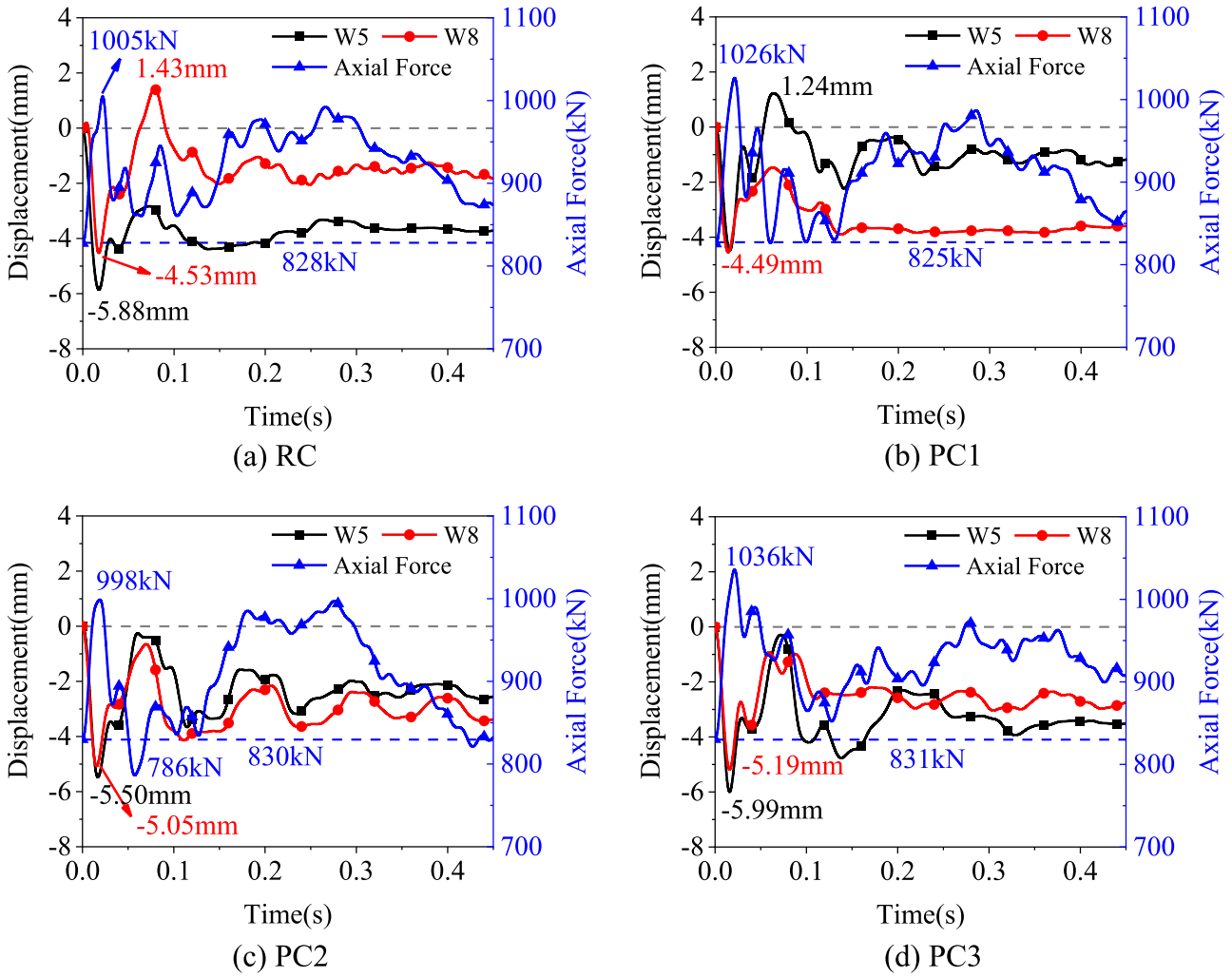

Fig. 14. The time history curves of axial force and vertical displacement.

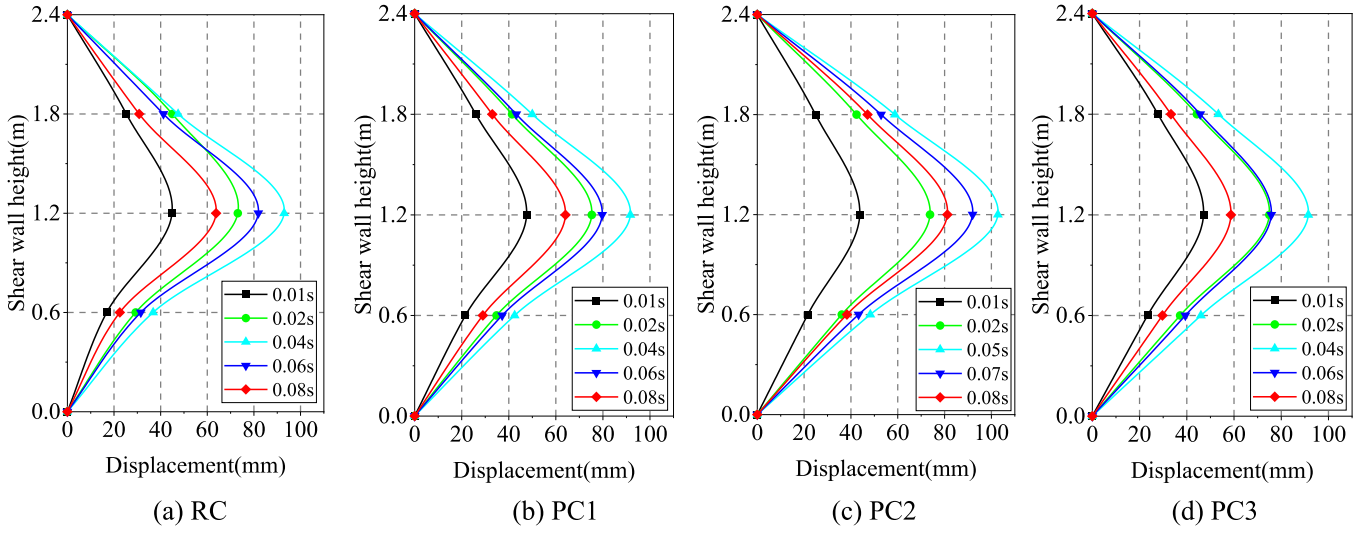

Fig. 15. Deformation curves.

similar trends, reaching peak values in a short period, followed by a significant decrease and subsequent generation of several peaks. It is noteworthy that the minimum values of inertia forces for PC1, PC2, and PC3 specimens are −424 kN, −427 kN, and −464 kN respectively, illustrating significant differences compared to the −286 kN of the RC specimen. This difference might be related to stiffness changes after the initial impact.

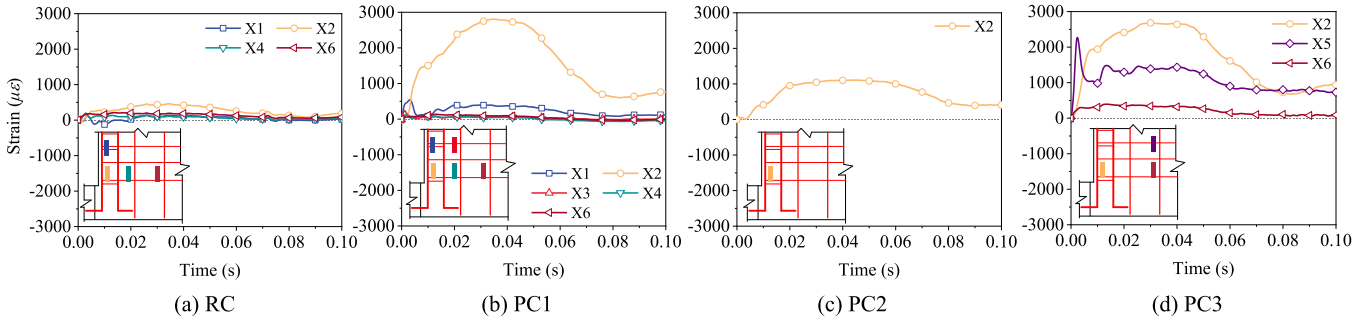

Fig. 16. Concrete strain histories on the impact-facing side.

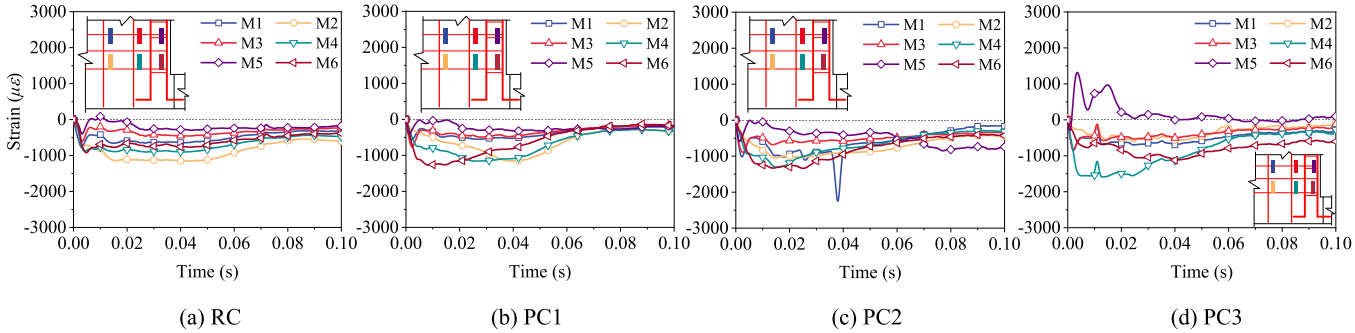

Fig. 17. Concrete strain histories on the back side.

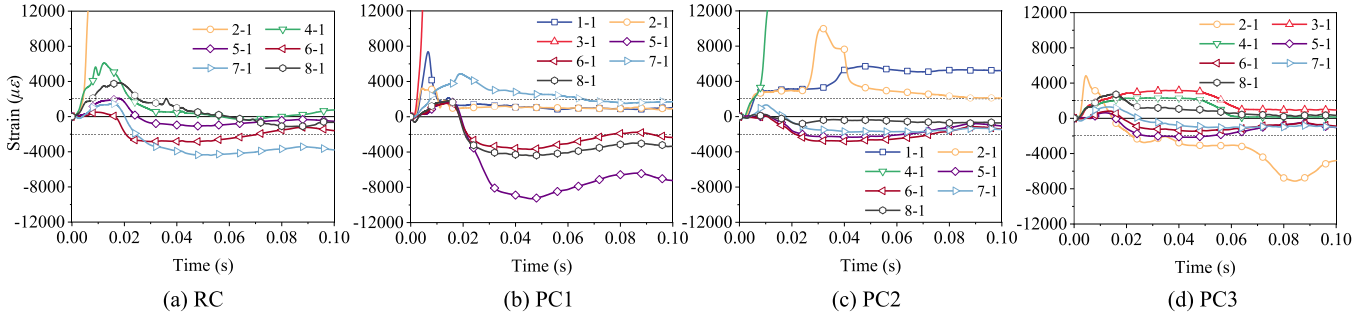

Fig. 18. Rebars strain histories on the impact-facing side.

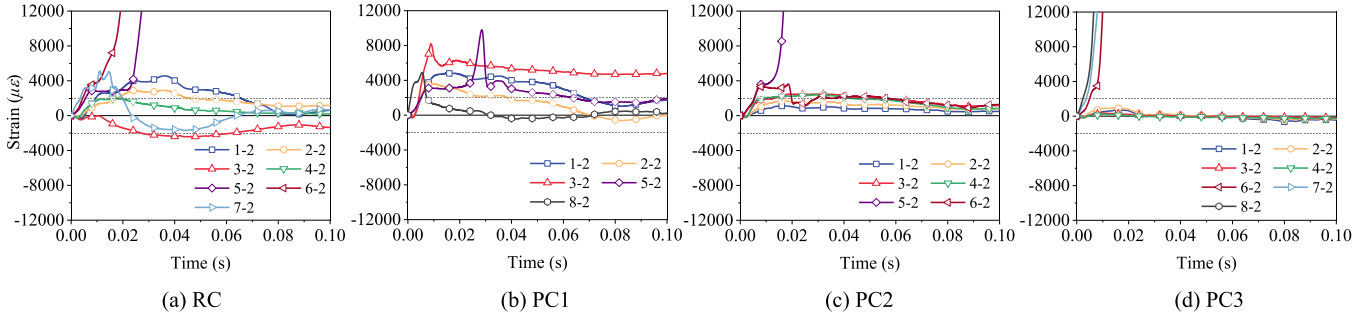

Fig. 19. Rebars strain histories on the back side.

5. Rapid evaluation method based on energy

It is difficult to determine the impact velocity and mass that structures may encounter in practical engineering scenarios. Design methods based on static conditions might overlook the inertial effects characterizing by the large peak magnitude and short duration of impact loads. Zhao et al. [51] proposed a simplified model to evaluate the dynamic shear requirements and capabilities of columns using Monte Carlo simulation and to analyze the reliability of columns under impact loads. Yi et al. [52] also proposed a two-mass model to simulate the dynamic response of RC beams under impact loads. Although these methods could effectively evaluate the impact resistance of reinforced concrete

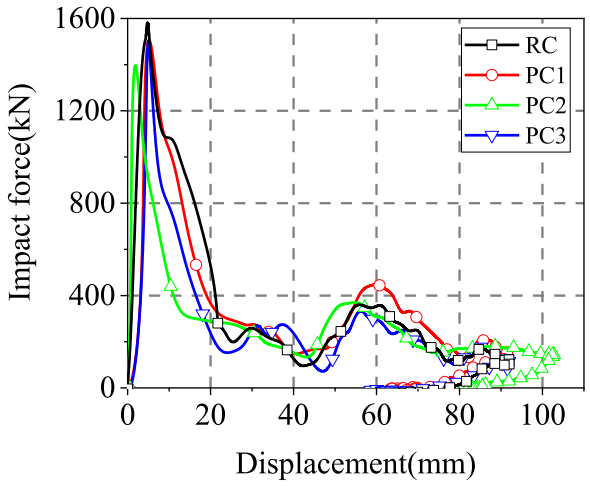

Fig. 20. Force-displacement curves.

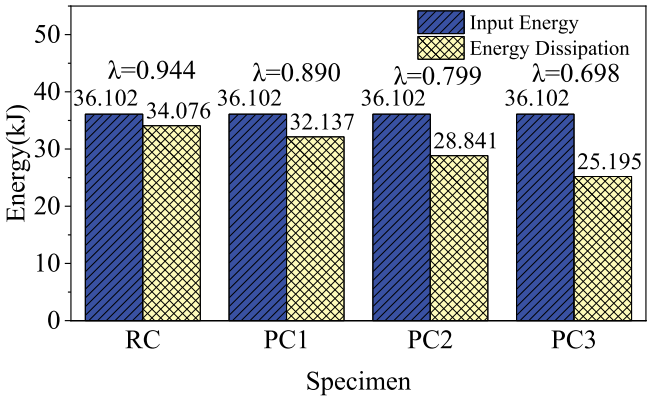

Fig. 21. Energy dissipation.

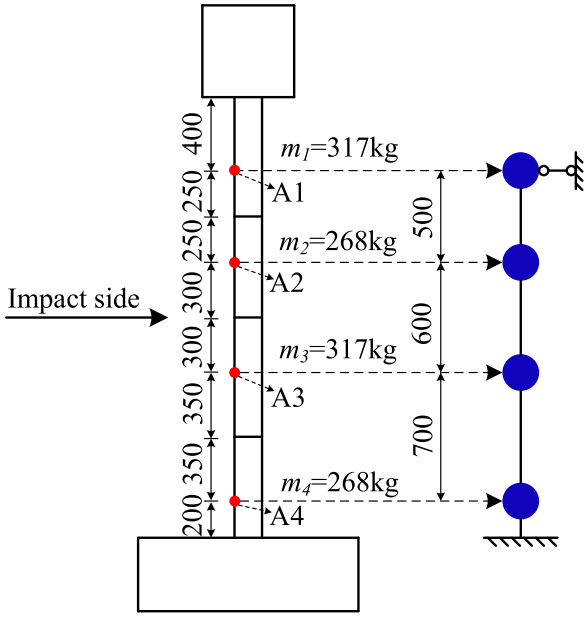

Fig. 22. Diagram of horizontal overall inertia force calculation.

components, a faster, simpler, and more effective evaluation method is still worth exploring.

Based on the research findings in Section 4.1, when subjected to out-of-plane impact loads, most of the energy is dissipated through deformation of the shear walls. Consequently, there may be a relationship between the impact energy and the deflection of the walls. A relevant study [49] also corroborates this hypothesis, demonstrating a linear increase in the maximum mid-span deflection of walls with the increase in impact energy, thus providing a framework for the evaluation of impact resistance. However, careful consideration of the maximum allowable deflection of the walls, δ_{max}, is necessary. This approach, combined with empirical formulas [53,54] and the literature [55], provided a rational method for the evaluation of impact resistance.

$$\delta_{\max} = \alpha \frac{E_{kd}}{P_{used}} \tag{8}$$

where $\delta_{\max}$ is maximum deflection of the wall, α is coefficients fitted according to the test, E_{kd} is the pendulum kinetic energy, and P_{used} is the static bearing capacity of the wall.

Based on Eq. (8), combined with the impact tests of the wall panel components, the α values for each specimen can be calculated as shown in Table 6.

Based on this experiment and other relevant impact tests on wall panels, the range of α values was generally between 0.5 and 0.7. For the RC, PC1, and PC3 specimen, the values of parameter α are close to each other, while the parameter α of the PC2 specimen is noticeably higher. This indicates that when the shear wall primarily exhibits flexural failure, PC and RC specimens can adopt the same value for α; however, when the shear wall experiences localized failure, the value of α needs to be appropriately increased. Therefore, to further consider the influence of different connection forms on parameter α, it is suggested to uniformly set parameter α to 0.75. Therefore, the following steps can be followed for the evaluation of impact resistance.

Firstly, according to specific usage requirements, the maximum allowable deflection $\delta_{\max}$ and the concentration force P_{used} is calculated by the plastic hinge line method.

Then, the energy E_{kd} is calculated by substituting into the equation:

$$E_{kd} = \frac{P_{used}\delta_{\max}}{\alpha} \tag{9}$$

Finally, the impact resistance of wall panels is reflected by calculating the energy E_{kd}.

6. Conclusions

This paper experimentally studied the influence of connection types on PC shear walls against impact loading. Three PC shear wall specimens with different connection types and one RC shear wall specimen were tested under constant axial compression imitating actual load conditions of engineering structures. Detailed findings are summarized as follows.

1. Under the impact loading, all specimens exhibited apparent flexural failure with cracks distributed mainly around plastic hinge lines accompanied by several radial cracks. The number of cracks in the RC specimen was significantly fewer than in the PC specimens. Different degrees of cracking were observed in the grout layers of the PC specimens, with severe local damage observed in PC2.
2. Under the identical impact energy conditions, the peak impact force of the RC specimen exceeded that of the PC specimens. Among them, the peak impact forces of the PC1 and PC3 specimens were close and significantly higher than that of the PC2 specimen. RC specimen possessed the highest stiffness, then the PC1 and PC3 specimens, with the PC2 specimen exhibited the lowest stiffness.
3. With same connection types, PC shear wall specimens and PC column specimens exhibited consistent trends for the impact force time

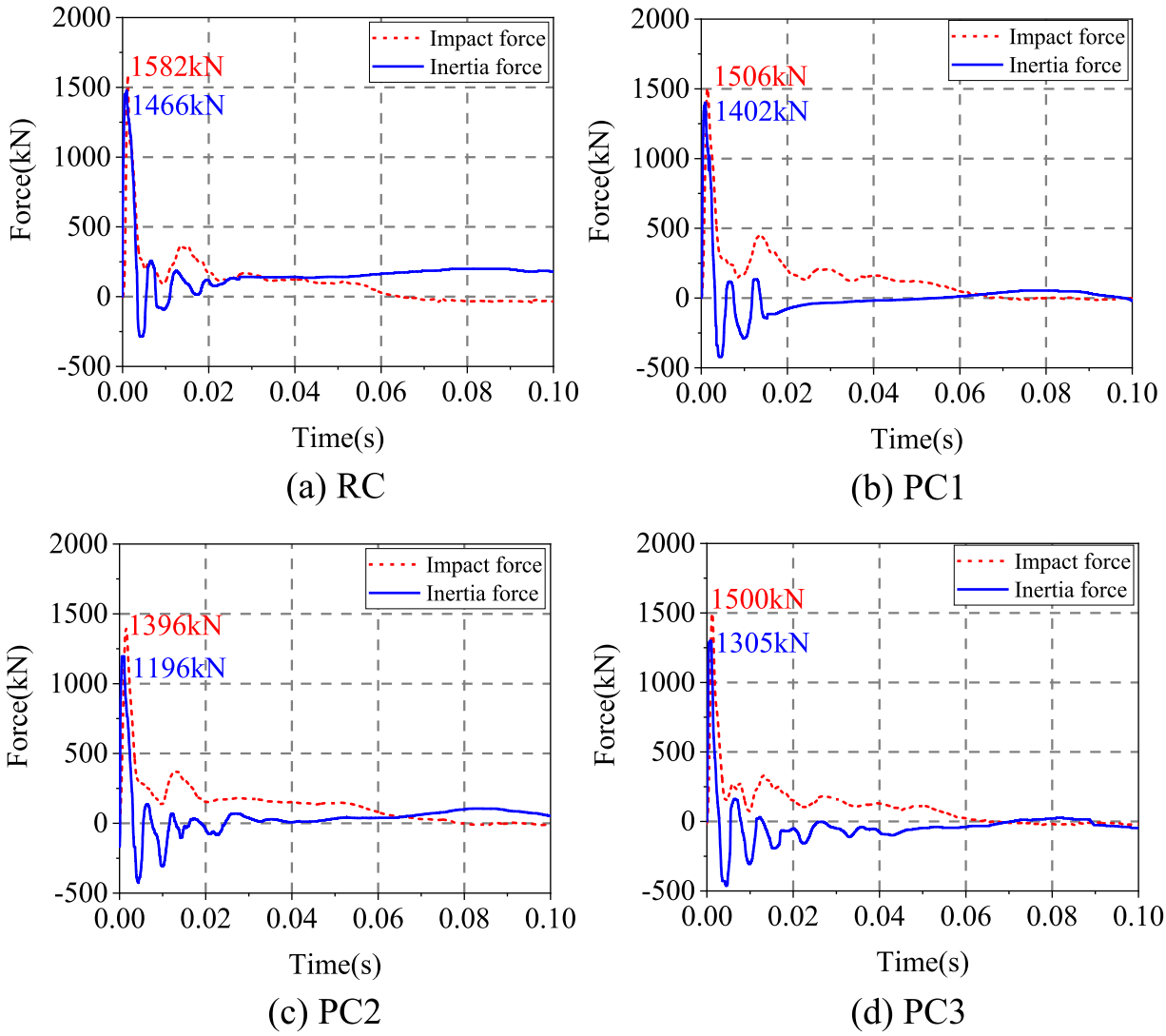

Fig. 23. Relationship of impact force and inertial force.

Table 6
Calculation results.

Specimen	Pendulum mass (kg)	Impact velocity (m/s)	Pendulum kinetic energy (J)	Static load-bearing capacity (kN)	Maximum deformation (mm)	Coefficient α
RC	2167	5.77	36073	241.5	92	0.62
PC1	2167	5.77	36073	241.5	91	0.61
PC2	2167	5.77	36073	241.5	103	0.69
PC3	2167	5.77	36073	241.5	92	0.62
[34] -A−1	640	3.83	4704	72.2	33	0.51
[34] -A−2	1140	3.83	8379	72.2	58	0.50
[34] -B−1	640	3.83	4704	81.2	37	0.64
[34] -B−2	1140	3.83	8379	81.2	53	0.51

history curve. However, shear wall specimens need longer time to reach the peak impact force, and their durations of overall impact force were shorter. This finding indicates the importance of distinguishing the types and structural characteristics of different components when designing and evaluating the impact resistance of buildings.

4. Edge members and axial compression force significantly enhanced the impact resistance of shear wall specimens in terms of maximum displacement and duration of impact force. The RC specimen and PC1 specimen exhibited a high degree of similarity on their stiffness, main rebars stress, and energy dissipation ratio. Under the premise of reliable grouting quality, it can be considered that the grouted sleeve connection is emulative to cast-in-situ construction when resisting impact loading.
5. A rapid energy-based evaluation method is developed to estimate the impact energy that wall panels can withstand. A recommended value of 0.75 for the parameter α is suggested based on experimental results. However, due to limited experimental data at present, this parameter in the proposed method might be calibrated achieving higher accuracy if more testing data are available.

CRediT authorship contribution statement

Wei-Jian Yi: Visualization, Supervision, Conceptualization. **Ting Li:** Investigation. **Fan Yi:** Visualization, Supervision. **Xin Zhang:** Writing – original draft, Validation, Formal analysis, Data curation. **Jia Ni:** Validation. **Jing-Ming Sun:** Writing – review & editing, Visualization, Methodology, Investigation, Conceptualization. **Yun Zhou:** Writing – review & editing, Methodology, Investigation, Funding acquisition, Conceptualization.

Declaration of Competing Interest

The authors declared that they have no conflicts of interest to this work.

Data availability

Data will be made available on request.

Acknowledgement

The authors sincerely appreciate the funding support provided by the National Natural Science Foundation of China (NSFC) (No. 51878264, No. 52278306), the Science and Technology Progress and Innovation Project of the Department of Transportation of Hunan Province (201912), the Natural Science Foundation of Hunan Province of China (No. 2023JJ70003), and the Hydraulic Science and Technology Project of the Hunan Provincial Department of Water Resources (No. XSKJ2023059–31).

References

[1] Xiao S, Wang ZL, Li XM, Harries K, Xu QF, Gao RD. Study of effects of sleeve grouting defects on the seismic performance of precast concrete shear walls. Eng Struct 2021;236:111833.
[2] Xue WC, Huang Q, Niu PY. Reversed cyclic tests on precast concrete shear walls with grouted corrugated metallic duct connections. Eng Struct 2022;256:113948.
[3] Xue WC, Huang Q, Li Y. Experimental study of precast concrete shear walls with spiral-confined lap connections under cyclic loads. J Build Eng 2022;52:104467.
[4] Xue WC, Huang Q, Gu XL, Hu X. Hysteretic behavior of precast concrete shear walls with steel sleeve-corrugated metallic duct hybrid connections. Structures 2022;38:820–31.
[5] Jiang JF, Luo J, Xue WC, Hu X, Qin D. Experimental study on hysteresis behavior of precast concrete double skin shear wall with horizontal loop connection and spiral-confined vertical lap connection. J Build Eng 2022;45:103526.
[6] Jiang JF, Xue WC, Luo J, Qin D. Hysteresis behavior of precast concrete composite shear walls with improved vertical connections. Structures 2022;36:533–48.
[7] Qian JR, Yang XK, Qin H, Peng YY, Zhang JM, Li JS. Tests on seismic behavior of pre-cast shear walls with various methods of vertical reinforcement splicing. J Build Struct 2011;32(6):51–9.
[8] Wu M, Liu HT, Du XL, Liu X. Seismic performance of precast short-leg shear wall using a grouting sleeve connection. Eng Struct 2020;208:110338.
[9] Yuan Q, Wang ZH, Li HH, Zhu HL, Suo N. Experimental study on seismic performance of new-type fabricated shear wall with mortar connection. J Build Eng 2021;43:103103.
[10] Pan GB, Cai J, He A, Chen QJ, Zuo ZL, He BQ, Tang XL, Wu HW. An experimental study of the seismic behaviour of precast concrete shear walls with bolted-plate connections. Eng Struct 2021;248:113203.
[11] Fan LZ, Wei JL, Chen Y, Feng J, Sareh P. Shear performance of large-thickness precast shear walls with cast-in-place belts and grouting sleeves. J Risk Uncertain Eng Syst 2023;9(2):04023005.
[12] Chen Y, Zhang Q, Feng J, Zhang Z. Experimental study on shear resistance of precast RC shear walls with novel bundled connections. J Earthq Tsunami 2019;13(3&4):1940002.
[13] Li WR, Gao HW, Xiang RJ, Du YF. Experimental study of seismic performance of precast shear wall with a new bolt-plate connection joint. Structures 2021;34:3818–33.
[14] Fu YQ, Fan GL, Tao L, Yang YJ, Wang JC. Seismic behavior of prefabricated steel reinforced concrete shear walls with new type connection mode. Structures 2022;37:483–503.
[15] Ding T, Xiao JZ, Wei KH, Lu YJ. Seismic behavior of concrete shear walls with bolted end-plate DfD connections. Eng Struct 2020;214:110610.
[16] Fan WY, Chen Y, Li JQ, Sun Y, Feng J, Hassanin H, Sareh P. Machine learning applied to the design and inspection of reinforced concrete bridges: Resilient methods and emerging applications. Structures 2021;33:3954–63.
[17] Suaris W, Shah SP. Properties of concrete subjected to impact. J Struct Eng 1983;109(7):1727–41.
[18] Banthia NP, Mindess S, Bentur A. Impact behavior of concrete beams. Mater Struct 1987;20(4):293–302.
[19] Bischoff PH, Perry SH. Impact behavior of plain concrete loaded in uniaxial compression. J Eng Mech 1995;121(6):685–93.
[20] Bentur A, Mindess S, Banthia N. The behaviour of concrete under impact loading: experimental procedures and method of analysis. Mater Struct 1986;19(5):371–8.
[21] Zineddin M, Krauthammer T. Dynamic response and behavior of reinforced concrete slabs under impact loading. Int J Impact Eng 2007;34(9):1517–34.
[22] Sadraie H, Khaloo A, Soltani H. Dynamic performance of concrete slabs reinforced with steel and GFRP bars under impact loading. Eng Struct 2019;191:62–81.
[23] Sengel S, Erol H, Yilmaz T, Anil O. Investigation of the effects of impactor geometry on impact behavior of reinforced concrete slabs. Eng Struct 2022;263:114429.
[24] Pham T, Hao H. Impact behavior of FRP-Strengthened RC beams without stirrups. J Compos Constr 2016;20(4):04016011.
[25] Pham T, Hao H. Plastic hinges and inertia forces in RC beams under impact loads. Int J Impact Eng 2017;103:1–11.
[26] Zhao DB, Yi WJ. Anti-impact behavior and design method for RC beams. J Vib Shock 2015;34(11):139–45.
[27] Chen L, Fang L, Fan W, Liu T, Wu H. Field test and numerical simulation of a full-scale RC pier under multiple lateral impacts. Eng Struct 2022;268:114747.
[28] Liu B, Fan W, Guo W, Chen BS, Liu R. Experimental investigation and improved FE modeling of axially-loaded circular RC columns under lateral impact loading. Eng Struct 2017;152:619–42.
[29] Sun JM, Yi WJ, Chen H, Peng F, Zhou Y, Zhang WX. Dynamic responses of RC columns under axial load and lateral impact. J Struct Eng 2022;149(1):04022210.
[30] Zhou Y, Yang JB, Luo XM, Hwang HJ, Chen H, Sun JM, Yi WJ, Kang SM. Pendulum impact loading tests of precast concrete columns with various column base connections. Eng Struct 2022;252:113736.
[31] Li HW, Chen WS, Huang ZJ, Hao H, Ngo T, Pham T, Yeoh KJ. Dynamic response of monolithic and precast concrete joint with wet connections under impact loads. Eng Struct 2022;250:113434.
[32] Wang F, Liu JB, Bao X, Li ST, An ZY. Experimental study of the resistance of RC walls with different transverse reinforcements subjected to large-scale rigid projectile impacts. Eng Struct 2022;251:113558.
[33] Shi CL, Zhang JG, Zhang JB, Shao F, Zhang YC, Zhang ML. Experimental study and numerical analysis on impact resistance of civil air defense engineering shear wall. Adv Civ Eng 2021:7376909.
[34] Shi X.D. Experiment and numerical analysis of reinforced concrete shear wall out-of-plane impact resistance. Master thesis, Hunan University, Changsha China, 2018.
[35] Ministry of Housing and Urban-Rural Development of China (MHURDOC). Code for design of concrete structures (GB50010–2010), Beijing: China Architecture and Building Press; 2016 [in Chinese].
[36] Jiang JF, Luo J, Xue WC, Hu X, Qin D. Seismic performance of precast concrete double skin shear walls with different vertical connection types. Eng Struct 2021;245:112911.
[37] Ministry of Housing and Urban-Rural Development of China (MHURDOC). Technical standard for assembled buildings with concrete structure (GBT51231–2016). Beijing: China Architecture and Building Press; 2016 [in Chinese].
[38] Ministry of Housing and Urban-Rural Development of China (MHURDOC). Technical specification for precast concrete structures (JGJ 1–2014). Beijing: China Architecture and Building Press; 2014 [in Chinese].
[39] Ministry of Housing and Urban-Rural Development of China (MHURDOC)., Technical Specification of Multi-story Building for Precast Concrete Wall-slab Structures with Bolt Connection (T/CECS809–2021). Beijing: China Architecture and Building Press; 2021 [in Chinese].
[40] General Administration of Quality Supervision, Inspection and Quarantine of the People's Republic of China. Metallic materials. Tensile testing: Method of test at room temperature (GB/T228.1–2021), Beijing: Standards Press of China; 2021 [in Chinese].
[41] Ministry of Housing and Urban-Rural Development of China (MHURDOC). Standard for evaluation of concrete compressive strength (GB/T50107–2010), Beijing: China Architecture and Building Press; 2010 [in Chinese].
[42] State Administration for Market Regulation. Test method of cement mortar strength (GB/T17671–2021), Beijing: Standards Press of China; 2021 [in Chinese].
[43] Ministry of Housing and Urban-Rural Development of China (MHURDOC). Standard for test method of basic properties of construction mortar (JGJ/T70–2009), Beijing: China Architecture and Building Press; 2009 [in Chinese].
[44] Zhao DB, Yi WJ, Kunnath SK. Shear mechanisms in reinforced concrete beams under impact loading. J Struct Eng 2017;143(9):04017089.
[45] Fujikake K, Li B, Soeun S. Impact response of reinforced concrete beam and its analytical evaluation. J Struct Eng 2009;135(8):938–50.
[46] Kishi N, Mikami H, Matsuoka KG, Ando T. Impact behavior of shear-failure-type RC beams without shear rebar. Int J Impact Eng 2002;27(9):955–68.
[47] Said A, Mouwainea E. Experimental investigation on reinforced concrete slabs under high-mass low velocity repeated impact loads. Structures 2022;35:314–24.
[48] Shi CL, Zhang JG, Wang XY, Liu FF, Chen WL, Ma ZH, Liang HZ, Zhao Y. Improving the impact resistance and antisplash of civil air defense wall: experiments and finite-element simulation. J Struct Eng 2022;149(2):04022238.
[49] Jin L, Xia MX, Zhang RB, Lin MF, Du XL. Computational modeling and dynamic response of reinforced concrete shear wall under out-of-plane impact loading. Int J Impact Eng 2023;172:104425.

[50] Sun JM, Chen H, Yi F, Ding YB, Zhou Y, He QF, Zhang WX, Yi WJ. Experimental and numerical study on influence of impact mass and velocity on failure mode of RC columns under lateral impact. Eng Struct 2024;314:118416.
[51] Zhao WC, Qian J. Resistance mechanism and reliability analysis of reinforced concrete columns subjected to lateral impact. Int J Impact Eng 2020;136:103413.
[52] Yi WJ, Zhao DB, Kunnath SK. Simplified approach for assessing shear resistance of reinforced concrete beams under impact loads. Acids Struct J 2016;113(4):747–56.
[53] Tachibana S, Masuya H, Nakamura S. Performance based design of reinforced concrete beams under impact. Nat Hazard Earth Sys 2010;10:1069–78.
[54] Kishi N, Mikami H. Empirical formulas for designing reinforced concrete beams under impact loading. Acids Struct J 2012;109(4):509–20.
[55] Yi WJ, Shi XD. Numerical simulation analysis for RC shear walls under impact load. J Vib. Shock 2019;38(13):102–10.